Invited Article: Nano-kirigami metasurfaces by focused-ion-beam induced close-loop transformation SCI

Zhiguang Liu, Huifeng Du, Zhi-Yuan Li, et al.

COLLECTIONS

View Online   Export Citation   CrossMark

ARTICLES YOU MAY BE INTERESTED IN

Dynamic metasurface lens based on MEMS technology
APL Photonics **3**, 021302 (2018); https://doi.org/10.1063/1.5018865

All-dielectric phase-change reconfigurable metasurface
Applied Physics Letters **109**, 051103 (2016); https://doi.org/10.1063/1.4959272

Mechanical metamaterials based on origami and kirigami
Applied Physics Reviews **8**, 041319 (2021); https://doi.org/10.1063/5.0051088

Invited Article: Nano-kirigami metasurfaces by focused-ion-beam induced close-loop transformation

Zhiguang Liu,[1,2] Huifeng Du,[3] Zhi-Yuan Li,[4,a] Nicholas X. Fang,[3,a] and Jiafang Li[1,a]

[1]*Institute of Physics, Chinese Academy of Sciences, Beijing 100190, China*
[2]*University of Chinese Academy of Sciences, Beijing 100049, China*
[3]*Mechanical Engineering Department, Massachusetts Institute of Technology, Cambridge, Massachusetts 02139, USA*
[4]*College of Physics and Optoelectronics, South China University of Technology, Guangzhou 510640, China*

Reducing fabrication difficulties while maintaining structural complexities and functionalities is one of the key challenges faced by the applications of nanophotonic devices. Here we demonstrate an exotic metasurface by using a simple close-loop nano-kirigami method. Based on the focused-ion-beam induced continuous shape transformation of a suspended ultra-thin gold film, pinwheel-like metasurfaces with uniaxial broadband polarization conversion and handedness-sensitive phase properties are readily fabricated. By deliberately patterning the metasurfaces periodically with opposite handedness, high-contrast cross-polarized diffractions are successfully observed in both linear and radial configurations. The demonstrated new types of metasurfaces, together with their suspended features for reconfiguration potentials, can open up new possibilities for the exploration of functional and reconfigurable micro-/nano-photonic and electronic devices. © *2018 Author(s).*
All article content, except where otherwise noted, is licensed under a Creative Commons Attribution (CC BY) license (http://creativecommons.org/licenses/by/4.0/).
https://doi.org/10.1063/1.5043065

I. INTRODUCTION

Metasurfaces,[1] a kind of two-dimensional (2D) artificial phase-engineered material with sub-wavelength thickness, have rapidly grown up in recent few years due to their intriguing capabilities on modulating the behaviors of electromagnetic waves and potential applications ranging from polarization control,[2,3] flat meta-lens,[4–6] metahologram,[7] angular momentum engineering,[8] and nonlinear frequency conversion.[9] Toward practical applications, recent advances in optical metasurfaces are focused on functionality multiplexing such as broadband and achromatic operation,[10–13] as well as the realization of reconfiguration/tunability.[14–17] In the latter aspect, more recent studies proposed to integrate optical metasurfaces on MEMS-based[18,19] and elastic platforms,[20] or with 2D materials,[21] phase change materials,[22] and transparent conducting oxide,[23] which, however, increased the fabrication or material complexities. One possible solution to these challenges is to extend the designs from ultra-thin 2D to three-dimensional (3D) space, i.e., to fabricate the metasurfaces into a directly configurable formation like those investigated in terahertz wavelength regions.[24] However, this increases the difficulties in nanofabrication and brings up challenges for the conventional bottom-up or top-down fabrication techniques.

Here we demonstrate an exotic metasurface by using a simple close-loop nano-kirigami method based on the focused-ion-beam (FIB) irradiation technique. This novel nano-kirigami method enables

---

[a]Authors to whom correspondence should be addressed: jiafangli@aphy.iphy.ac.cn; phzyli@scut.edu.cn; and nicfang@mit.edu

3D nanostructures with uniaxial broadband polarization conversion and handedness-sensitive phase properties. By deliberately patterning the metasurfaces with different handedness, high-contrast cross-polarized diffractions are successfully observed in both linear and radial configurations. The demonstrated new types of metasurfaces, with their potentials in electronic and mechanical tuning, can open up new possibilities for the exploration of versatile and reconfigurable micro-/nano-photonic devices.

II. SAMPLE FABRICATIONS

As a direct machining tool with resolution down to several nanometers, FIB-based nanofabrication is usually accompanied by residual stress, surface damage, or ion implantation, which have long been considered as drawbacks for applications such as transmission electron microscope (TEM) sample preparation and diagnosis.[25] Remarkably, we recently developed a nano-kirigami method by making good use of this "undesirable" residual stress.[26] The basic nano-kirigami transformation mechanism is that when the gold thin film (with a thickness of ~80 nm) is exposed to low-dose and uniform FIB irradiation, the vacancies introduced by ion collisions cause gentle surface roughness and at the same time induced tensile stress close to the film surface due to the grain coalescence. Meanwhile, some gallium ions are implanted and the affected gold atoms are dislocated, resulting in compressive stress.[25,27–29] The combination of the two stresses determines the net stress within the ion-beam-affected top layer, which deforms the rest bottom layer. Subsequently, the redistribution and equilibrium of such heterogeneous tensile stress result in the folding or bending of nanostructures similar to macroscopic paper-cuts and mesoscopic origami/kirigami.[30,31] Therefore, the FIB illumination schemes dramatically influence the nanofabrication results. Specifically on the one hand, there are two types of scanning schemes for the FIB irradiation, i.e., the local line-scanning irradiation and the global frame-scanning irradiation, which cause rigid folding[32–34] and gradual
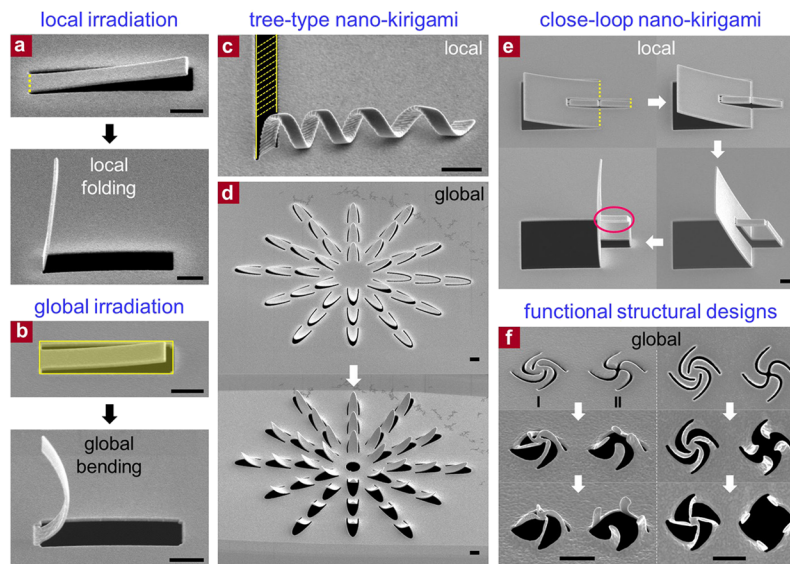

FIG. 1. SEM images of structures with FIB-based nano-kirigami. (a) Local irradiation of the suspended cantilevers under line-scanning along the dashed line with FIB, which induces rigid folding with zero curvatures. (b) Global irradiation of the suspended cantilevers under frame-scanning over the suspended area with FIB, which induces gradual bending with continuous curvatures. [(c) and (d)] Tree-type nano-kirigami of a twisted spiral and a flower-shaped structure under local and global FIB irradiation, respectively. (e) Close-loop nano-kirigami of a pop-up plate under parallel local FIB irradiation along the multiple dashed lines. (f) (Left) Side-view and (right) top-view of two arc patterns under global FIB irradiation. The arcs in the type-I pattern are untouched, which results in the rising and twisting of a pinwheel structure under close-loop nano-kirigami. In comparison, the arcs in the type II pattern are connected, which results in the global bending of a four-pillar structure under the tree-type nano-kirigami. The arrows indicate the increasing direction of FIB irradiation dosage. Thickness of the gold film: 80 nm. Scale bar: 1 μm.

bending of the micro-stripe, respectively, as shown in Figs. 1(a) and 1(b). On the other hand, being dependent on the 2D pattern designs and from the viewpoint of topological classifications, the FIB-based nano-kirigami can be sorted into two types,[26] i.e., the tree-type and close-loop nano-kirigami. In the tree-type nano-kirigami, as shown in Figs. 1(c) and 1(d), each subunit is relatively independent of the other ones during the shape transformation processes in both cases of local irradiation and global irradiation. The second type is the so-called close-loop nano-kirigami, in which the relative motion of one object influences the motions of the others and vice versa. As illustrated in Fig. 1(e), when the FIB irradiation scans along the three dashed lines in a parallel loop, the part noted by the red ellipse is passively actuated by other inter-connected folding parts even without FIB irradiation at its two ends, clearly reflecting the feature of close-loop transformation.

When coming to functional nanostructures, the close-loop and tree-type nano-kirigami methods make a big difference as well. As shown in the top of Fig. 1(f), two types of 2D arc structures (type I and type II) are designed and fabricated on a suspended gold film, which merely have a tiny difference in the center part before nano-kirigami. Specifically, the four arcs of the type II pattern are connected with each other and divide the structure into four isolated parts, which leads to the global bending and popping-up effect of each part without interrelated changes; i.e., a four-pillar structure is obtained by the tree-type nano-kirigami [bottom of Fig. 1(f)]. In comparison, the four arcs in the type I pattern remain disconnected and keep the structure unified, which results in the interrelated popping-up, twisting, and rotation during the global FIB irradiation; i.e., a pinwheel-like structure is obtained by the close-loop nano-kirigami. The dramatic difference of the structural evolution in Fig. 1(f) clearly demonstrated the significance brought by close-loop nano-kirigami.

III. POLARIZATION AND PHASE PROPERTIES OF METASURFACES

The significance of the close-loop nano-kirigami is reflected not only in visual images but also in optical properties. As the spectra shown in Fig. 2(b), under x-polarized incidence, the pinwheel-like structures [type I design in Fig. 2(a)] arranged in a square lattice periodicity of 1.45 μm exhibit strong cross-polarized (y-polarized) transmission for wavelengths larger than 1.45 μm, with a sharp resonance peak around 1.55 μm. In comparison, the four-pillar structures [type II design in Fig. 2(a)] obtained by tree-type nano-kirigami possess little cross-polarization effects. The fundamental reason is that the twisted features of the pinwheel-like structure allow for 3D electric current loops,[35,36] with which parallel electric and magnetic moments can be induced by the electromagnetic field of incident light. The interaction between electric and magnetic moments causes different phase delays for right-handed and left-handed circularly polarized (RCP and LCP) light. As a result, the polarization direction of linearly polarized light (can be seen as the superposition of RCP and LCP light) is rotated and strong cross-polarization conversion is observed.[26]

Besides strong polarization conversion, the pinwheel-like structures also possess interesting handedness-related transmission phases. As illustrated in Fig. 2(c), the simulated distributions of the transmitted y-polarized electric field (Ey) show a phase difference of π between the left-handed (LH) and right-handed (RH) pinwheel structures for wavelengths at 1.5, 1.6, and 2.0 μm, respectively. More detailed simulations in Fig. 2(d) show that such a π-phase difference exists for all the wavelengths larger than 1.45 μm, where the cross-polarized conversion occurs. In comparison, the phase of x-polarized transmission remains the same for both LH and RH structures. As shown in Fig. 2(e), the LH and RH pinwheels possess strong linear polarization rotation under x-polarized excitation without making the polarization elliptical and the rotation angles have a relationship of $\theta_L = -\theta_R = \theta$. In such a case, the Jones matrix of the LH and RH pinwheels can be written as

$$M_L = Te^{i\beta}\begin{pmatrix} \cos\theta & -\sin\theta \\ \sin\theta & \cos\theta \end{pmatrix} \text{ and } M_R = Te^{i\beta}\begin{pmatrix} \cos\theta & \sin\theta \\ -\sin\theta & \cos\theta \end{pmatrix}, \tag{1}$$

where T is the transmission coefficient and β is the phase retardation. For x-polarized incidence, the transmitted field can be expressed as

$$\begin{pmatrix} E_{x,L} \\ E_{y,L} \end{pmatrix}_{out} = M_L E_{in} = Te^{i\beta}\begin{pmatrix} \cos\theta & -\sin\theta \\ \sin\theta & \cos\theta \end{pmatrix}\begin{pmatrix} 1 \\ 0 \end{pmatrix} = Te^{i\beta}\begin{pmatrix} \cos\theta \\ \sin\theta \end{pmatrix}, \tag{2}$$
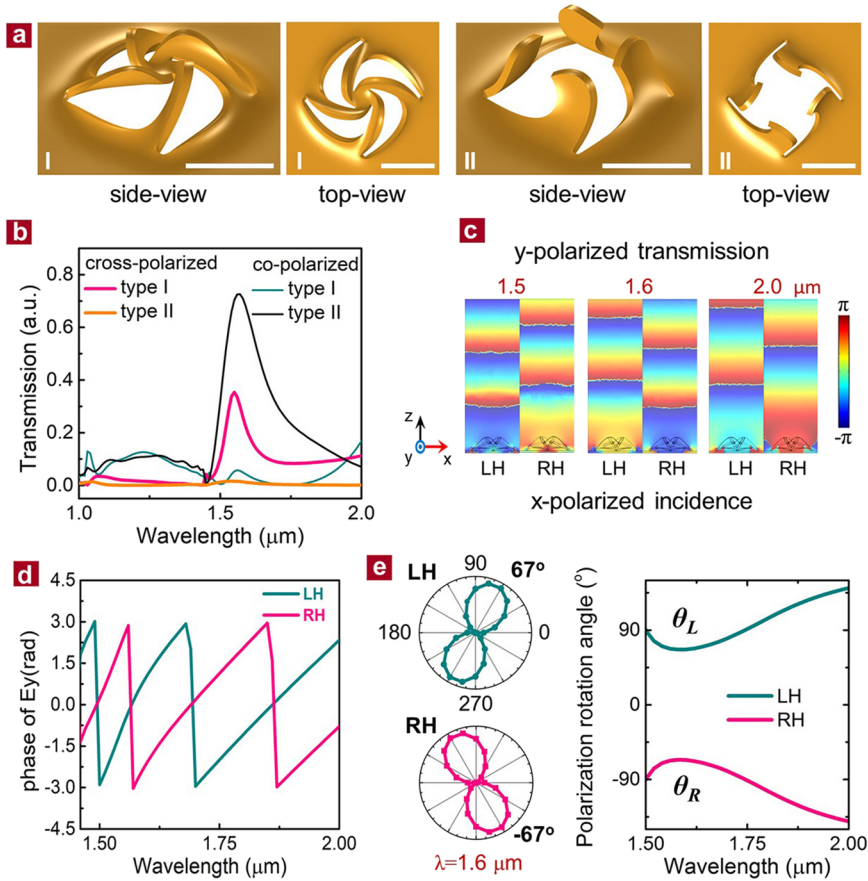
FIG. 2. Calculated optical properties of structures after nano-kirigami. (a) Schematic of the pinwheel (type I) and four-pillar (type II) structures after close-loop and tree-type nano-kirigami, in good replica of the structural shapes in Fig. 1(f). Scale bar: 500 nm. (b) Co-polarized (x-polarized) and cross-polarized (y-polarized) transmission of type I and type II structures, respectively, with a square lattice period of 1.45 μm under x-polarized incidence. (c) Phase diagram of the transmitted y-polarized electric-field (Ey) in the xz plane at wavelengths of 1.50, 1.60, and 2.00 μm, respectively, for pinwheels with left-handed (LH) and right-handed (RH) rotation. (d) Transmission phase spectra of Ey for LH and RH pinwheels, respectively. It can be seen that the phase differences between LH and RH remains constantly around π for all wavelengths above the lattice period. (e) (Left) Polar plots of calculated transmission versus detection polarization angle at 1.6 μm under x-polarized incidence for the LH and RH pinwheels, respectively. It can be seen that the LH pinwheels rotate the polarization in the anti-clockwise direction by 67°, while the RH pinwheels rotate the polarization by −67° in the clockwise direction. (Right) Calculated linear polarization rotation angle (θ) versus wavelength for the LH and RH pinwheels, respectively. It can be seen that $\theta_L = -\theta_R$ exists for all the wavelengths from 1.5 to 2.0 μm.

$$\begin{pmatrix} E_{x,R} \\ E_{y,R} \end{pmatrix}_{out} = M_R E_{in} = T e^{i\beta} \begin{pmatrix} \cos\theta & \sin\theta \\ -\sin\theta & \cos\theta \end{pmatrix} \begin{pmatrix} 1 \\ 0 \end{pmatrix} = T e^{i\beta} \begin{pmatrix} \cos\theta \\ -\sin\theta \end{pmatrix}. \tag{3}$$

Therefore, one obtains $E_{y,R} = e^{i\pi} E_{y,L}$, which confirms a phase difference of π between the LH and RH pinwheels for the cross-polarized transmitted field.

IV. DIFFRACTIVE PROPERTIES OF METASURFACES

To demonstrate the numerical predictions, LH and RH pinwheel-like arrays with a lattice periodicity of 1.45 μm were successfully fabricated through the FIB-based close-loop nano-kirigami method. As shown in Fig. 3(a), the measured co-polarized (x-polarized) transmission and cross-polarized (y-polarized) transmission under normal incidence with x-polarized excitation are well consistent with the numerical calculations in Fig. 2(b), and strong polarization conversion is observed in structures with both handedness. By further arranging the LH and RH pinwheels alternately
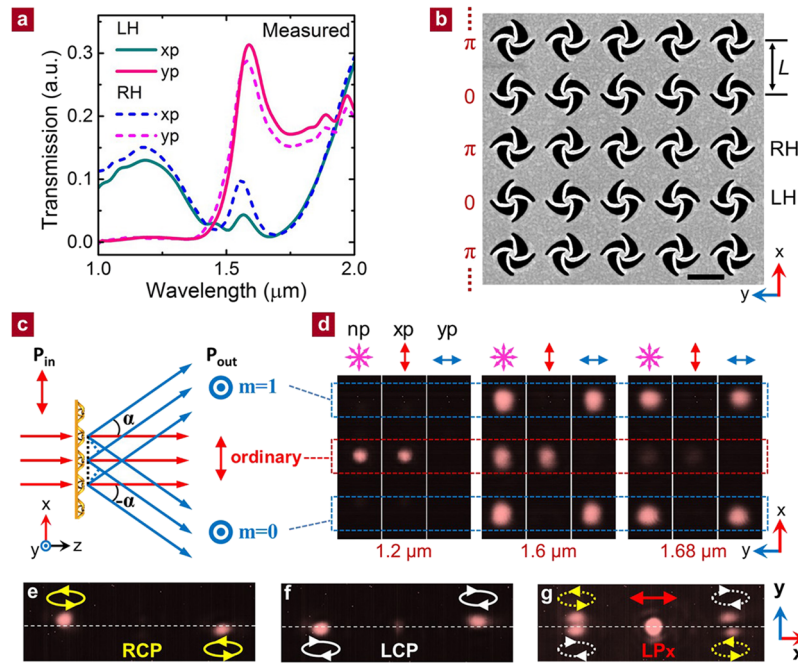
FIG. 3. Experimental phase and polarization manipulation. (a) X-polarized (xp) and y-polarized (yp) transmission spectra of LH and RH pinwheel arrays, respectively, under x-polarized incidence. (b) Top-view SEM image of a linear grating in which the LH and RH pinwheels fabricated alternately along the x-direction. Lattice and grating period: $L = 1.45 \, \mu$m. For the y-polarized transmission, there is a phase shift of π along the x-direction, as noted at the left side of the SEM image. Scale bar: 1 μm. (c) Schematic of the diffraction properties of the linear grating in the xz plane under x-polarized incidence. The ordinary beam propagating in the z-direction keeps the original x-polarization. The converted y-polarized (cross-polarization) light is diffracted with angle $-\alpha$ and α for m = 0 and 1, respectively. (d) CCD camera images of the transmitted light spots at wavelengths of 1.20, 1.60, and 1.68 μm, respectively, under detection with non-polarization (np), x-polarization (xp), and y-polarization (yp). Dashed rectangles outline the correspondence of the imaging spots to each beam. The diffraction spots are expected to exist at wavelengths from 1.45 to 2.0 μm, where the cross-polarized transmission is non-zero. [(e) and (f)] CCD images of the spots of the diffracted RCP and LCP beams under the illumination with LCP and RCP incident light, respectively. (g) CCD images of the beam spots with both incident and detection polarization aligned along the x-direction. Dashed circles indicate the positions of the equivalent RCP and LCP diffraction spots. The illumination power and imaging time in (g) are increased compared to other images.

with a periodicity of L (1.45 μm) along the x-axis, a binary diffractive grating is readily manufactured, as shown in Fig. 3(b). In such a case, under the same x-polarized excitation, the transmitted cross-polarized (y-polarized) light from pinwheel structures with different handedness will have the same amplitude but with a phase shift of π, as illustrated at the left side of Fig. 3(b). According to diffraction theory, the transmitted cross-polarized beams (y-polarized light) will be diffracted by an angle α [Fig. 3(c)] that satisfies $L \sin \alpha = (m - 1/2)\lambda$, where $m = 0, \pm 1, \pm 2, \ldots$, while the ordinary x-polarized transmission will maintain the incident direction. When the windmill period L is smaller than the operation wavelength λ, the value of m can only be 0 or 1, as schematically plotted in Fig. 3(c). These characteristics are well verified by the recorded camera images in Fig. 3(d). For example, at a wavelength of 1.6 μm, the center spot corresponding to the ordinary transmission appears under x-polarized detection, while the top and bottom spots corresponding to the diffractive beams show y-polarization. In comparison, only the center spot is observed at a wavelength of 1.2 μm since the cross-polarized transmission is nearly zero [Fig. 3(a)]. On the contrary, at a wavelength of 1.68 μm, the center spot is hardly seen since most of the light is converted into the diffracted beams with y-polarization. Therefore, at this wavelength, the polarization rotation angle reaches at around 90° and the ratio between cross-polarized to co-polarized transmission exceeds 15:1, as consistently plotted in Fig. 3(a).

It should be mentioned that the diffractive polarization conversion is not only working with linearly polarized incidence but also applicable to the circularly polarized waves; i.e., the phase

gradient in Fig. 3(b) is also applicable to circular polarization conversion. For example, at a wavelength of 1.68 μm, the diffractive cross-polarized RCP and LCP light spots are formed under LCP and RCP incident waves [Figs. 3(e)–3(f)], respectively, although the polarization conversion efficiency is weak. Moreover, despite the spots being diffracted along the x-axis due to the phase modulation in Fig. 3(b), the imaging spots move slightly along the y-direction. Interestingly, the shifting direction is opposite between the RCP and LCP spots. Since the phase distribution is merely modulated along the x-axis [Fig. 3(b)], this y-direction shift is thus perpendicular to the changing direction of the dielectric constant and could be regarded as the intriguing photonic spin Hall effect (SHE)[37–39] that comes from the spin-orbit interaction of light. To verify this effect, a much intensive x-polarized light (can be seen as the superposition of an LCP wave and an RCP wave) is used to excite the sample and the detection polarization is set to the x-direction to eliminate the strong y-polarized diffraction. As a result, the positions of the diffraction spots equivalent to the cross-polarized RCP and LCP waves are clearly identified in Fig. 3(g). The equivalent RCP/LCP diffraction spots are oppositely shifted along the y-direction, respectively, which is in good agreement with those recorded in Figs. 3(e)–3(f). The behind mechanism is that the drastic phase gradient in the x-direction breaks the axial symmetry of the interface and makes the diffractive light propagate along a curved trajectory. To satisfy the momentum conservation, a geometric polarization rotation is introduced, which depends on the helicity of incident light. As a result, the spin-orbit interaction changes the path of circularly polarized light at the direction perpendicular to the phase gradient, which leads to the light spots of opposite handedness moving to the opposite directions, as shown in Figs. 3(e)–3(g).[39,40]

Since the pinwheel structures possess four-fold (C4) rotational symmetry on the z-axis, their polarization and phase properties are expected to be uniaxial for normal incident light, which is
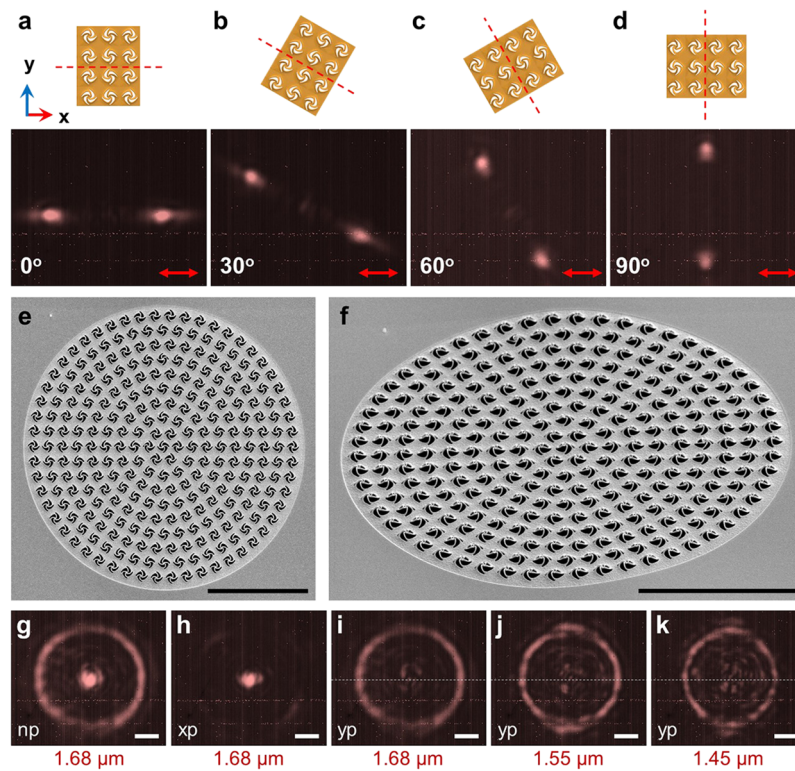

FIG. 4. Diffractive gratings. [(a)–(d)] Schematic and recorded diffraction images of linear grating with different orientation angles with respect to the incident polarization direction. The incident and detection polarizations are fixed at the x-polarized and y-polarized directions, respectively. [(e) and (f)] Top-view and side-view SEM images of a circular grating with the radiation separation of $\Delta r = 1.45\ \mu$m. [(g)–(k)] CCD camera images of transmitted light with np, xp, and yp detections under x-polarized incidence at wavelengths of 1.45, 1.55, and 1.68 μm, respectively. White dashed lines in [(i)–(k)] indicate the central position of the diffracted circular rings, where the center spot with original polarization is absent. Scale bars: 10 μm.

unique compared with the anisotropic subunits of many metasurface designs. Therefore, the cross-polarized diffraction works for arbitrary linearly polarized light and the diffraction plane can be rotated by simply rotating the orientation of the grating, as shown in Figs. 4(a)–4(d). Moreover, since the phase change is an intrinsic characteristic of the pinwheel structures, the grating design can be extended from linear to circular arrangement without rotating the direction of the unit cell. As illustrated in Figs. 4(e) and 4(f), by patterning LH and RH pinwheel structures alternatively in the radial direction, a radial diffractive grating is readily fabricated. Similar to the linear grating, the cross-polarized transmitted electric field has a phase difference of π between LH and RH structures along every adjacent rings. As a result, in the diffractive images obtained under x-polarized incidence, the transmitted light with original x-polarization shows a spot at the center [Figs. 4(g) and 4(h)]. In comparison, the diffracted beams (with m = 0 and 1) under y-polarized detection overlap and form a bright ring, as shown in Figs. 4(g) and 4(i). Moreover, it is found that the cross-polarized bright rings exist in broadband, as shown in Figs. 4(i)–4(k), as expected since the phase difference between LH and RH structures is constant for wavelengths larger than 1.45 μm [Fig. 2(d)].

V. DISCUSSIONS AND CONCLUSIONS

In this article, we have demonstrated an exotic metasurface by employing a simple close-loop nano-kirigami method, which is based on the FIB enabled continuous shape transformation of a suspended ultra-thin gold film. Pinwheel-like metasurfaces with 3D twisting features are readily fabricated, which possess strong polarization conversion and handedness-sensitive phase properties due to the interactions between the induced electric and magnetic moments. By utilizing the constant phase difference of π between the pinwheel structures of opposite handedness, high-contrast cross-polarized diffractions are successfully observed in both linear and radial configurations. Moreover, the phase characteristic is an intrinsic property of the uniaxial pinwheel structures, which allows for the diffractive polarization conversion applicable to versatile arrangements such as linear and radial gratings. In such a case, unlike the anisotropic linear grating, the radial grating is an isotropic device and can operate at an arbitrary polarization angle. The scheme has great potentials as well, for example, to be applied in various thin-films, such as aluminum and commercial silicon nitride thin films. With such a nano-kirigami principle, large-scale fabrication is also possible with other fabrication strategies (results not shown). Furthermore, the suspending features of the metasurfaces possess potential applications in reconfigurable nanophotonic and optomechanical devices by actuating the suspended subunits with external stimulus such as electrostatic and thermal tuning. Therefore, the uniaxial broadband polarization conversion capability of the demonstrated metasurfaces, as well as their design and fabrication principles, provides a novel solution to the active configuration of flexible metasurfaces and other versatile micro-/nano-photonic and electronic devices.

VI. METHODS

A. Numerical simulations

The transmission spectra and phase distributions of the 3D pinwheels were calculated using the finite-element-method (FEM). Periodic boundary conditions were applied to the corresponding edges of the unit cell structure in x- and y-axes. The plane wave was produced from the port in xy plane and propagated along the z-axis direction, which has the same configuration as the experiments. The phase monitor was placed at 4 μm behind the structures, and an averaged operation was used to obtain the results.

B. Sample fabrications

All the structures were fabricated by using a focused-ion-beam system (FEI Helios 600i) on free-standing gold films. The 80 nm-thick gold film suspended on copper mesh was provided by the lift-off process in previous studies.[34] For the nano-kirigami method, the 2D curves were first cut by the FIB under doses of >600 pC/μm^2. Second, global or local ion-beam irradiations were conducted

with doses of ~10-40 pC/μm^2. The acceleration voltage and current beam of Ga$^+$ were set at 30 kV and 24 pA, respectively.

C. Optical characterizations

The optical measurements were performed by using a homemade spectroscopy system. Two near-infrared (NIR) objective lens ($\times$10, NA 0.25, Olympus and $\times$100, NA 0.9, Olympus) were adopted to focus incident light (HL-2000, Ocean Optics) onto the sample and collect transmitted signals, respectively. The transmissions were detected by using a spectrometer (SP-2300, Princeton Instruments) equipped with a liquid nitrogen cooled CCD detector (PyLoN-IR). A NIR CCD camera (XS-4406, Xenics) was adopted for capturing the diffraction images.

ACKNOWLEDGMENTS

[1] N. Yu, P. Genevet, M. A. Kats, F. Aieta, J.-P. Tetienne, F. Capasso, and Z. Gaburro, Science **334**, 333 (2011).

[2] Y. Zhao and A. Alu, Nano Lett. **13**, 1086 (2013).

[3] P. C. Wu, W. Y. Tsai, W. T. Chen, Y. W. Huang, T. Y. Chen, J. W. Chen, C. Y. Liao, C. H. Chu, G. Sun, and D. P. Tsai, Nano Lett. **17**, 445 (2017).

[4] M. Khorasaninejad, W. T. Chen, R. C. Devlin, J. Oh, A. Y. Zhu, and F. Capasso, Science **352**, 1190 (2016).

[5] B. H. Chen, P. C. Wu, V. C. Su, Y. C. Lai, C. H. Chu, I. C. Lee, J. W. Chen, Y. H. Chen, Y. C. Lan, C. H. Kuan, and D. P. Tsai, Nano Lett. **17**, 6345 (2017).

[6] Y. E. Geints and A. A. Zemlyanov, J. Opt. **20**, 075102 (2018).

[7] G. X. Zheng, H. Muhlenbernd, M. Kenney, G. X. Li, T. Zentgraf, and S. Zhang, Nat. Nanotechnol. **10**, 308 (2015).

[8] G. X. Li, M. Kang, S. M. Chen, S. Zhang, E. Y. B. Pun, K. W. Cheah, and J. S. Li, Nano Lett. **13**, 4148 (2013).

[9] G. Li, S. Zhang, and T. Zentgraf, Nat. Rev. Mater. **2**, 17010 (2017).

[10] W. T. Chen, K. Y. Yang, C. M. Wang, Y. W. Huang, G. Sun, I. D. Chiang, C. Y. Liao, W. L. Hsu, H. T. Lin, S. Sun, L. Zhou, A. Q. Liu, and D. P. Tsai, Nano Lett. **14**, 225 (2014).

[11] S. M. Wang, P. C. Wu, V. C. Su, Y. C. Lai, C. H. Chu, J. W. Chen, S. H. Lu, J. Chen, B. B. Xu, C. H. Kuan, T. Li, S. N. Zhu, and D. P. Tsai, Nat. Commun. **8**, 187 (2017).

[12] Y. D. Hou, H. M. Leung, C. T. Chan, J. L. Du, H. L. W. Chan, and D. Y. Lei, Adv. Funct. Mater. **26**, 7807 (2016).

[13] S. M. Wang, P. C. Wu, V. C. Su, Y. C. Lai, M. K. Chen, H. Y. Kuo, B. H. Chen, Y. H. Chen, T. T. Huang, J. H. Wang, R. M. Lin, C. H. Kuan, T. Li, Z. L. Wang, S. N. Zhu, and D. P. Tsai, Nat. Nanotechnol. **13**, 227 (2018).

[14] S. Walia, C. M. Shah, P. Gutruf, H. Nili, D. R. Chowdhury, W. Withayachumnankul, M. Bhaskaran, and S. Sriram, Appl. Phys. Rev. **2**, 011303 (2015).

[15] Q. Wang, E. T. F. Rogers, B. Gholipour, C. M. Wang, G. H. Yuan, J. H. Teng, and N. I. Zheludev, Nat. Photonics **10**, 60 (2016).

[16] H. H. Hsiao, C. H. Chu, and D. P. Tsai, Small Methods **1**, 1600064 (2017).

[17] K. Chen, Y. J. Feng, F. Monticone, J. M. Zhao, B. Zhu, T. Jiang, L. Zhang, Y. Kim, X. M. Ding, S. Zhang, A. Alu, and C. W. Qiu, Adv. Mater. **29**, 1606422 (2017).

[18] E. Arbabi, A. Arbabi, S. M. Kamali, Y. Horie, M. Faraji-Dana, and A. Faraon, Nat. Commun. **9**, 812 (2018).

[19] T. Roy, S. Zhang, I. W. Jung, M. Troccoli, F. Capasso, and D. Lopez, APL Photonics **3**, 021302 (2018).

[20] A. She, S. Y. Zhang, S. Shian, D. R. Clarke, and F. Capasso, Sci. Adv. **4**, eaap9957 (2018).

[21] P. C. Wu, N. Papasimakis, and D. P. Tsai, Phys. Rev. Appl. **6**, 044019 (2016).

[22] C. H. Chu, M. L. Tseng, J. Chen, P. C. Wu, Y. H. Chen, H. C. Wang, T. Y. Chen, W. T. Hsieh, H. J. Wu, G. Sun, and D. P. Tsai, Laser Photonics Rev. **10**, 986 (2016).

[23] Y. W. Huang, H. W. H. Lee, R. Sokhoyan, R. A. Pala, K. Thyagarajan, S. Han, D. P. Tsai, and H. A. Atwater, Nano Lett. **16**, 5319 (2016).

[24] H. Tao, A. C. Strikwerda, K. Fan, W. J. Padilla, X. Zhang, and R. D. Averitt, Phys. Rev. Lett. **103**, 147401 (2009).

[25] M. J. Samayoa, M. A. Haque, and P. H. Cohen, J. Micromech. Microeng. **18**, 095005 (2008).

[26] Z. Liu, H. Du, J. Li, L. Lu, Z.-Y. Li, and N. X. Fang, "Nano-kirigami with giant optical chirality," Sci. Adv. **4**, eaat4436 (2018).

[27] W. D. Nix and B. M. Clemens, J. Mater. Res. **14**, 3467 (1999).

[28] W. J. Arora, S. Sijbrandij, L. Stern, J. Notte, H. I. Smith, and G. Barbastathis, J. Vac. Sci. Tech. B **25**, 2184 (2007).

[29] W. J. Arora, H. I. Smith, and G. Barbastathis, Microelectron. Eng. **84**, 1454 (2007).

[30] G. P. Collins, Proc. Natl. Acad. Sci. U. S. A. **113**, 240 (2016).

[31] Y. H. Zhang, F. Zhang, Z. Yan, Q. Ma, X. L. Li, Y. G. Huang, and J. A. Rogers, Nat. Rev. Mater. **2**, 17019 (2017).

[32] A. J. Cui, Z. Liu, J. F. Li, T. H. H. Shen, X. X. Xia, Z. Y. Li, Z. J. Gong, H. Q. Li, B. L. Wang, J. J. Li, H. F. Yang, W. X. Li, and C. Z. Gu, Light: Sci. Appl. **4**, e308 (2015).

[33] Z. Liu, J. Li, Z. Liu, W. Li, J. Li, C. Gu, and Z.-Y. Li, Sci. Rep. **7**, 8010 (2017).

[34] Z. G. Liu, Z. Liu, J. F. Li, W. X. Li, J. J. Li, C. Z. Gu, and Z. Y. Li, Sci. Rep. **6**, 27817 (2016).

[35] Z. J. Wang, L. Q. Jing, K. Yao, Y. H. Yang, B. Zheng, C. M. Soukoulis, H. S. Chen, and Y. M. Liu, Adv. Mater. **29**, 1700412 (2017).

[36] R. Zhao, L. Zhang, J. Zhou, T. Koschny, and C. M. Soukoulis, Phys. Rev. B **83**, 035105 (2011).

[37] M. Onoda, S. Murakami, and N. Nagaosa, Phys. Rev. Lett. **93**, 083901 (2004).

[38] X. B. Yin, Z. L. Ye, J. Rho, Y. Wang, and X. Zhang, Science **339**, 1405 (2013).

[39] X. H. Ling, X. X. Zhou, K. Huang, Y. C. Liu, C. W. Qiu, H. L. Luo, and S. C. Wen, Rep. Prog. Phys. **80**, 066401 (2017).

[40] K. Y. Bliokh, A. Niv, V. Kleiner, and E. Hasman, Nat. Photonics **2**, 748 (2008).